Nanoscale measurement with pattern recognition of an ultra-precision diamond machined polar microstructure

Chenyang Zhao, Chi Fai Cheung*, Mingyu Liu

State Key Laboratory of Ultra-precision Machining Technology, Department of Industrial and Systems Engineering, The Hong Kong Polytechnic University, Hung Hom, Kowloon, Hong Kong, China

*Corresponding author: Benny.Cheung@polyu.edu.hk

ABSTRACT: Due to the low resolution of pattern recognition and disorganized textures of the surfaces of most natural objects observed under a microscope, computer vision technology has not been widely applied in precision positioning measurement on machine tools, which needs high resolution and accuracy. This paper presents a systematic method to solve the surface recognition problem which makes use of ultra-precision diamond machining to produce a functional and polar-coordinate surface named 'polar microstructure'. The unique characteristic of a polar microstructure is the distinctive pattern of any locations including rotation in the global surface which provides the feasibility of achieving precise absolute positions by matching the patterns by utilizing computer vision technology. A polar microstructure which possesses orientation characteristics is also able to measure the displacement of rotation angle. A series of simulation experiments including feature point extraction, orientation detection as well as resolution of pattern recognition was conducted, and the results show that a polar microstructure can achieve a resolution of 9.35 nm which is capable of providing a novel computer vision-based nanometric precision measurement method which can be applied in positioning on machine tools in the future.

Key words: Polar microstructure; Computer vision; Ultra-precision machining; Nanoscale measurement; Pattern recognition

1. Introduction

Currently, there are many principles of precision positioning measurement such as time-of-flight distance principle, absolute laser interferometer principle, surface encoding principle [1], etc. One of the common features of the above principles is that the strict requirements for their components and the environment such as a vacuum is needed to control the above uncertainty source, [2-4]. The space and operation convenience of the above devices also need improvements. Considering the rapid development of computer vision [5-8], it is a good idea to use the improvement of algorithms in robustness and accuracy to partially replace the rigorous requirements for the physical properties of measurement equipment. Computer vision has been used in various fields such as face recognition [9], astronomy [10], target tracking [11], cryptography [12], etc. Much

research has focused on improving the speed and robustness of computer vision and has achieved great success [13-15]. However, there are few related surveys on improving the resolution and precision of computer vision because most of the applied fields of computer vision are of macroscopic size. Moreover, resolution and precision are necessary to be considered in precision measurement. In order to improve the resolution, microscopic observation of the target is an important solution, but it causes difficulty to have a high resolution of pattern recognition on most natural object surfaces. In addition, regularity and reproducibility of the surface are also the important considerations. Generation of textured surface with high resolution of pattern recognition to the nanometer level is a core and tough issue. Ultra-precision machining (UPM) technology aims to achieve surface roughness with form accuracy in the range of sub-micrometer and a few nanometers [16-20]. In this paper, an integrated ultra-precision machining and computer vision method are used for precision measurement. The block diagram of the proposed technique is as shown in Fig. 1.

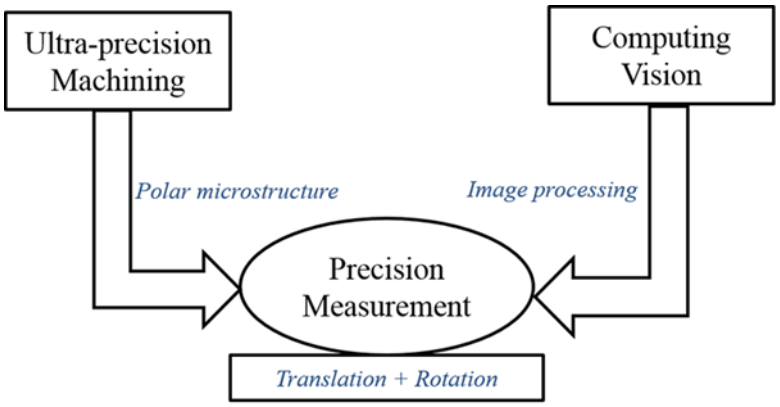

Fig. 1 A framework of the integrated ultra-precision machining and computer vision method

UPM has been applied in many areas such as aerospace, semiconductors, medical, optics, etc. UPM with computer vision is a great combination for the generation of a desirable functional surface. A process chain system in UPM as shown in Fig. 2 is used in this paper to propose the functional microstructure surface with high resolution of pattern recognition.

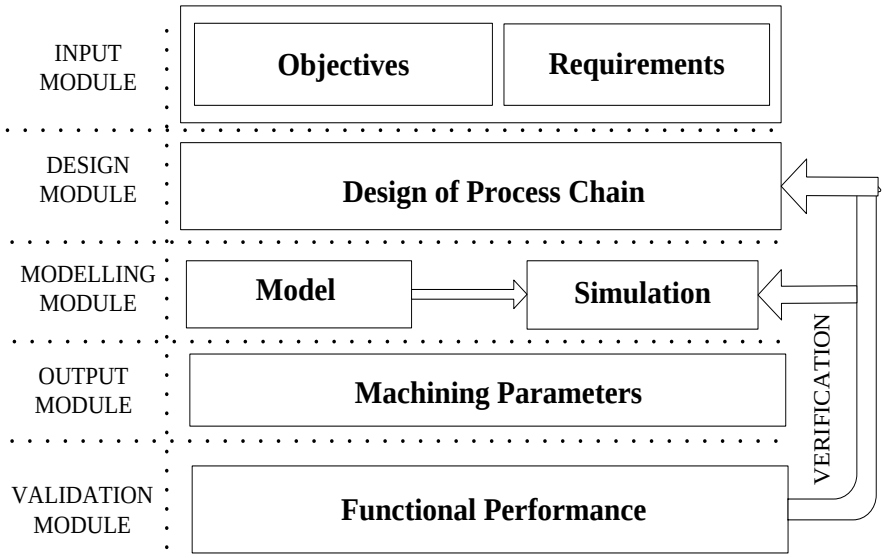

Fig. 2 A schematic diagram of the design of the process chain system for ultra-precision machining polar microstructures

As shown in Fig 1, the objective is to machine a micro-structured surface to achieve feature distinction at the nanometer level which provides some invariance to geometric and photometric differences. Considering the objectives, Fig. 3 summarizes the requirements of the microstructure. In regard to computer vision, for the further considerations, this microstructure should have the function to be detected by the rotation angle displacement and the microstructure should have an obvious orientation. Furthermore, the microstructure surface should have enough and uniform features for subsequent matching. Considering the situation in this paper, there should be at least two feature points anywhere under the vision field of a microscope, but more feature points help to improve the matching accuracy [10]. In regard to UPM, in order to have greater advantages than the current precision measurement methods, the microstructure should possess high machining efficiency with high reproducibility at a low cost.

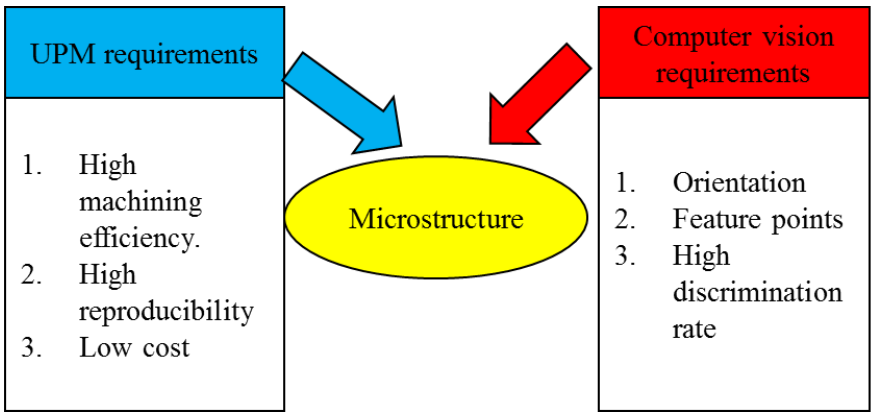

Fig. 3 Requirements of microstructure surface

2. Design of the polar microstructure

Briefly, the principle of computer vision-based precision measurement is to firstly capture a microscopic image above the microstructure surface, and the absolute position of the captured image on the global microstructure surface is then determined. Hence, the original positioning information is in the form of images. Consequently, the original positioning data are images. Generally, a grayscale image is a two-dimensional exhibit $A(m \times n)$:

$$\begin{bmatrix} a_{11} & a_{12} & \cdots & a_{1n} \\ a_{21} & a_{22} & \cdots & a_{2n} \\ \cdots & \cdots & \cdots & \cdots \\ a_{m1} & a_{m2} & \cdots & a_{mn} \end{bmatrix}_{m \times n}.$$

The number (m,n) means rows and columns of the 2-D array which refers to the pixel number in the vertical (m) and horizontal (n) directions respectively of the grayscale image. The element value a_{uv} in the array refers to the intensity value I of the pixel (u,v), where $a_{uv} \in [0,255]$. According to Euclidean distance shown as Eq. (1) [6]:

$$D(\theta_i) = \{\sum_{j=0}^{m-1} [A_1(\theta_j) - A_2(\theta_j + \theta_i)]^2\}^{\frac{1}{2}}, \tag{1}$$

where $D(\theta)$ is the Euclidean distance, θ is the rotation angle of array A, and i and j represent the initial and incremental stage respectively. One feasible solution of the array A is expressed as Eq. (2):

$$A = [W..BW..BW..W]_n, \tag{2}$$

where $W = [255...255]_m^T$, $B = [0...0]_m^T$. Its physical expression is shown in Fig. 4(a).

In UPM, single point diamond broaching (SPDB) is chosen to machine the microgrooves because of its high efficiency. More importantly, SPDB and the next machining process can be performed by the same machine tool. The spacing of two adjacent broaching grooves is 50 μm which guarantees significant orientation features at the microscale as illustrated in Fig. 4(b).

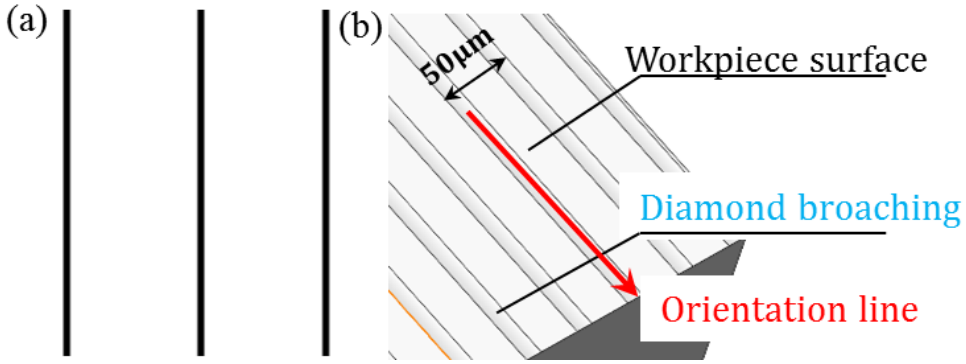

Fig. 4 Orientation line of microstructure (a) Physical express (b) Machining process

Besides the orientation, to register two images, there is a need to find a transformation model that can transform the geometry of one image to resemble the geometry of the other. To find a suitable transformation model, a set of locally unique points is selected from each image, correspondence is established between points in the images, and from the coordinates of homologous points, the parameters of the transformation model to register the images are determined. As local geometric differences between the images increase, a larger number of homologous points are required to account for the increased geometric differences among the images. Sufficient homologous points are obtained to compute the parameters of a transformation model, and there is a need to find a sufficiently large number of feature points in each image.

A feature point represents the center of a dark or bright blob, the point of intersection of two or more straight edges, the point of locally maximum curvature along an edge contour, or the center of a unique neighborhood in an image. To obtain adequate and uniform feature points, there should be a subsequent machining process to form uniform intersection points with SPDB. Moreover, considering the needed high resolution of pattern recognition, the formed pattern is necessary to be non-periodic, which is very different from the previous research which mostly uses periodic pattern and phase difference principles for precision measurement. In the second machining process, single point diamond turning (SPDT) is used to machine the concentric grooves with the same machine tool (Moore Nanotech 350FG) as that of SPDB. The final design of the polar microstructure is shown in Fig. 5.

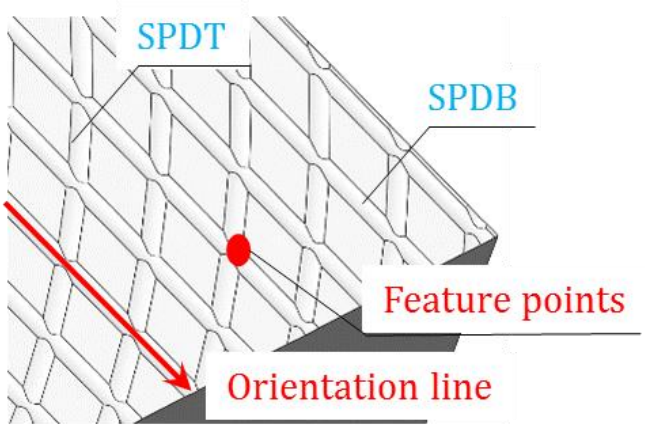

Fig. 5 Design of the polar microstructure

The designed microstructure is named ‘polar microstructure’ because it looks like a polar coordinate. Mostly, the visual field of a microscope is larger than a square visible area which is 100 μm x 100 μm, and each area in the polar microstructure in this area is unique. This means that the grayscale intensity distribution of this area is unique. In addition, the precision manufacturing process of the polar microstructure is only undertaken by a single machine tool, which avoids positioning errors caused by machine tool transfer during machining; therefore, it is highly efficient and accurate as well as creating low machining difficulty for machining polar microstructures to obtain a unique micro-structured surface.

Fig. 6 shows the machining steps with reference to the design principles. Ps is the spacing distance of straight grooves, Δs is the offset of straight groove from the machining circle center of the workpiece which solves the problem of the same appearance after being rotated 180 degrees. P_r is the spacing distance between concentric grooves.

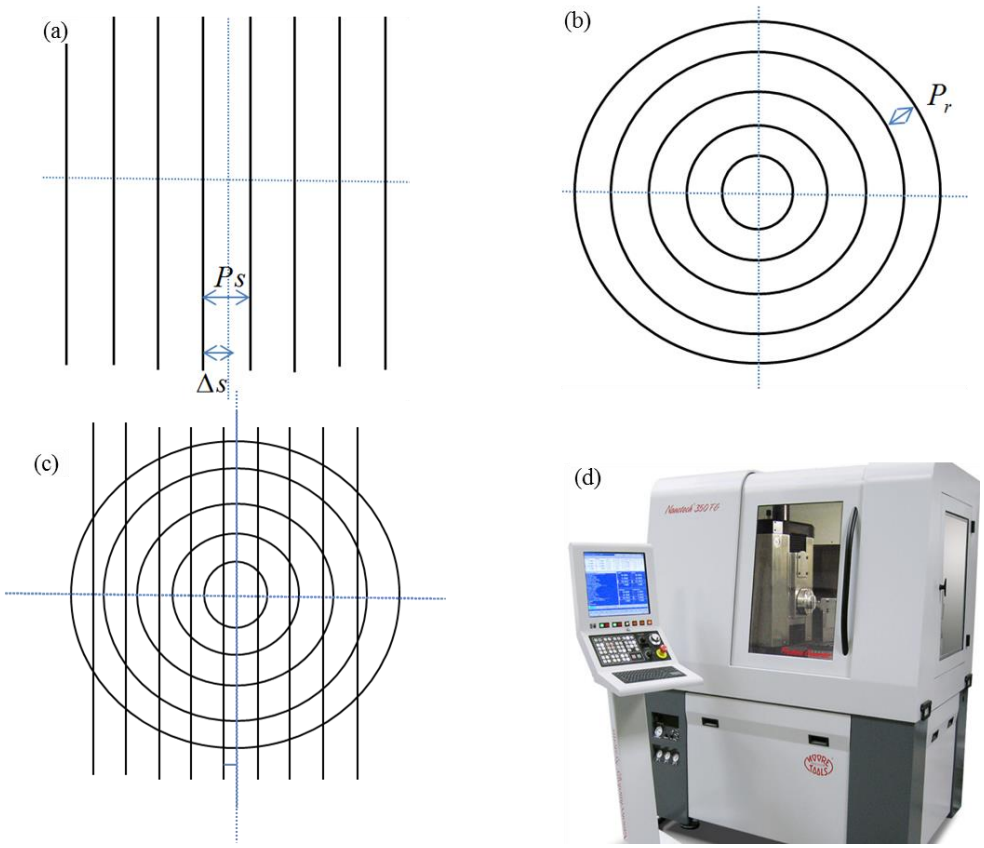

Fig. 6 Machining steps with reference to the design principles. a) The first machining process which broaches straight grooves. b) The second machining process is turning round grooves. c) Formative mixed surface texture after the above machining process chain. d) Machining equipment: Nanoform 350G from Nanotechnology Inc., USA.

3. Modeling and manufacturing of micro-structured surface

Considering modeling of the designed machining process chain associated with the machining process SPDB and SPDT, all the previous machining processes contribute and result in the final surface topography. Concisely, considering any point on the workpiece, the surface height h_{chain} ultimately depends on the lowest height of h_{pre}, h_{con} and h_{str}, which can be mathematically defined as Eq. (3):

$$h_{chain} = \arg\max_{(x,y)\in R}\{h_{pre}, h_{con}, h_{str}\} \tag{3}$$

where R is the total area on the workpiece surface, h_{pre} refers to the surface height of the pre-machined workpiece, h_{str} represents the surface height of straight grooves machined with SPDB and h_{con} refers to the surface height of circular grooves machined with SPDT. The machining parameters are optimized and chosen as experimental parameters as shown in Table I. The workpiece material in machining the polar microstructure is nickel-copper. The workpiece was diamond

machined by an ultra-precision machining system named Nanoform 350G. In fact, diamond-machined materials such as aluminum and copper are applicable for the machining of polar microstructures. Fig. 7 shows a comparison between the designed model (see Fig, 7(a)) and experimental results measured with a microscope (see Fig, 7(b)). Simulated surface topography and measured surface topography are compared in Fig. 6(c) and Fig. 6(d). It is interesting to note that under UPM, polar microstructures have great productivity which improves the reliability for mass production in the future.

Table I Machining parameters of the polar microstructure

Pre-machining process (Rough turning)	Spindle speed: r/min	3,000
	Feed rate: mm/min	2
	Depth of cut: um	5
Machining straight grooves (SPDB)	Feed rate of broaching straight grooves (mm/min)	800
	Feed rate of reaching workpiece (mm/min)	10
	Feed rate of leaving workpiece (mm/min)	400
	Depth of cut: um	5
	Δs (μm)	10
	p_s (μm)	50
	Number of straight grooves:	250
Machining round grooves (SPDT)	Duration time of machining round grooves (s)	3
	Feed rate of reaching workpiece (mm/min)	10
	Feed rate of leaving workpiece (mm/min)	400
	Depth of cut: um	5
	p_r (μm)	50
	Number of round grooves:	250
	The radius of the smallest round groove	100

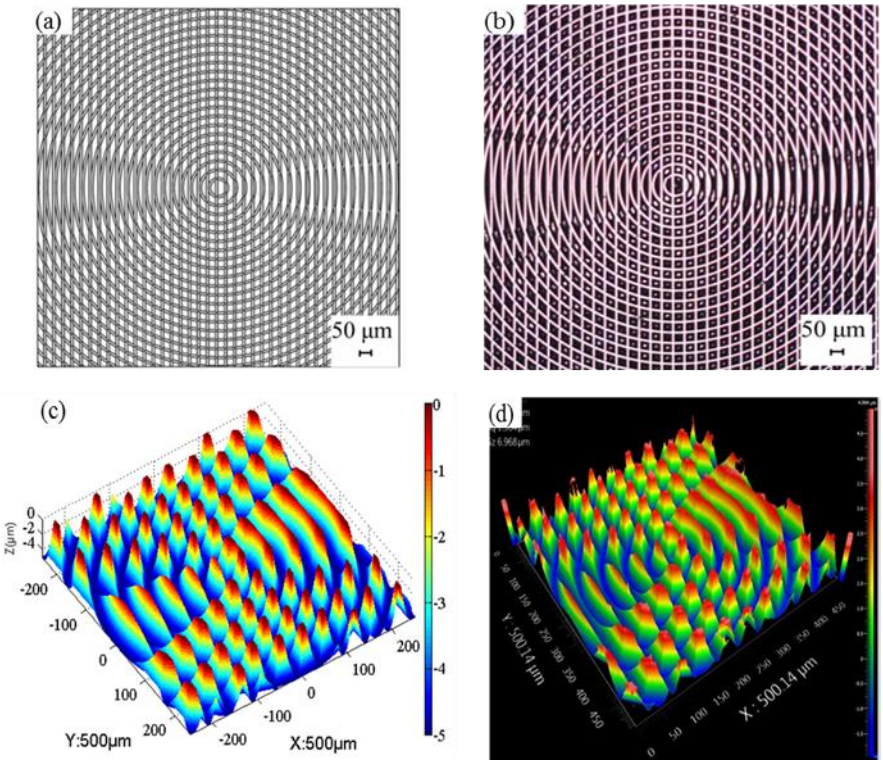

Fig. 7 Comparison between simulation results and measured results of the polar microstructure. a) Top view from the workpiece center. b) Corresponding area with Fig. 7a) measured with a Pearl Centering Microscope. c) Simulated surface topography. d) Corresponding area with Fig. 7c) measured with a Zygo^{TM} interferometer.

4. Performance validation

Based on the objectives and requirements of polar microstructures, a series of experiments was conducted to test the following capability of polar microstructures: feature point extraction, orientation and resolution of pattern recognition. In the validation experiments, the polar microstructure workpiece was placed on the optical surface profiler (Zygo ^{TM}) as shown in Fig. 8.

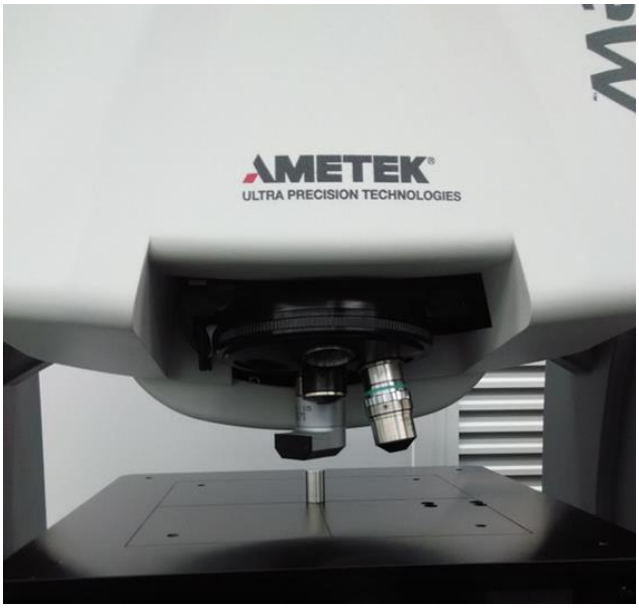

Fig. 8 Experimental setup

4.1 Feature point extraction

The central moments method to detect feature points was utilized [21, 22]. Considering a small $n \times n$ window centered at (x_0, y_0) in grayscale image $I(x, y)$, the central moment of order pq of the window is defined by Eq. (4):

$$\mu_{pq}^{I}(x_0, y_0) = \sum_{x=x_0-n/2}^{x_0+n/2} \sum_{y=y_0-n/2}^{y_0+n/2} (x - x_0)^p (y - y_0)^q I(x, y) \quad , \tag{4}$$

where p and q are nonnegative integers. The moments are computed with respect to the center of the window and within a square window in order not to favor the x-coordinates more than or less than the y-coordinates when detecting points.

To detect more distinct neighborhoods in an image, instead of intensity I in Eq. (4), intensity gradient magnitude I_g is used calculated from Eq. (5) to Eq. (7):

$$I_g(x, y) = \{I_x^2(x, y) + I_y^2(x, y)\}^{1/2} \quad , \tag{5}$$

$$I_x(x, y) = I(x+1, y) - I(x, y) \quad , \tag{6}$$

$$I_y(x, y) = I(x, y+1) - I(x, y) \quad , \tag{7}$$

where $I_x(x, y)$ is the gradient in the x-direction and $I_y(x, y)$ is the gradient in the y-direction at (x, y).

Based on the central momentum algorithm, Fig. 9 shows the feature point extraction result performed. It can be noticed from Fig. 9(b) that the detected feature points are separated uniformly on the surface of the polar microstructure. An enlarged view is shown in Fig. 9(c). Feature points are concentrated on the intersection points of SPDT and SPDB, which indicates that the machining process of the polar microstructure meets the requirement of generating uniform and enough feature points. Moreover, it is interesting to note in Fig. 9(b) that not all feature points can be determined as well as that of Fig. 9(c). There are a few feature points which do not coincide with the locations of the machining intersection points exactly. This is caused by many factors such as the machining quality, imaging quality as well as the algorithm error. However, this has little influence on the subsequent measurement accuracy because not only are there enough detected feature points for subsequent matchings, but also the images are all captured on the same manufactured polar microstructure surface; therefore, the accuracy of actual feature point locations can be guaranteed in different-view images. Overall, the polar microstructure is

competent to provide enough, uniform and accurate feature points for measurement matching.

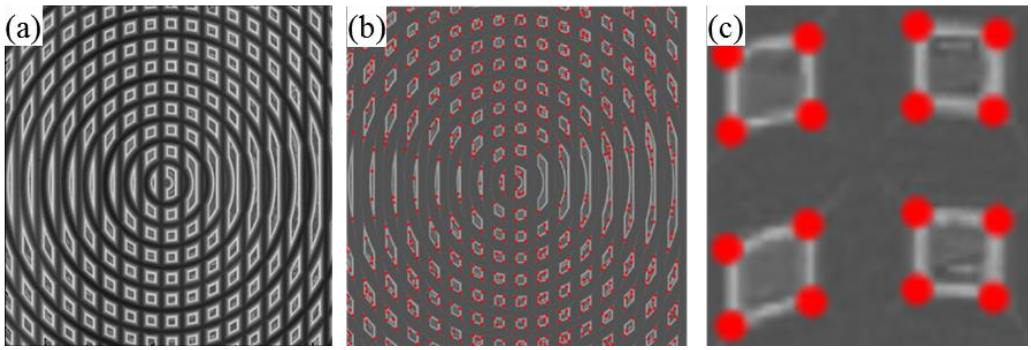

Fig. 9 Feature point extraction result (a) Original image (b) Feature point extraction result (c) An enlarged area of the feature point extraction result

4.2 Orientation

The determination of orientation is firstly based on the edge detection method which has been investigated extensively [23-25] and is not described in this paper. This paper gives a brief description of the orientation detection principle based on edge detection. Given a sequence of pixels along an edge contour, it can be expressed by Eq. (8) [23]:

$$\mathbf{P} = \{\mathbf{p}_i = (x_i, y_i) : i = 0, ..., n-1\}, \tag{8}$$

the parametric curve approximating the contour takes the form as shown in Eq. (9) [23]:

$$\mathbf{p}(u) = [x(u), y(u)], \tag{9}$$

the rational Gaussian (RaG) curve approximating the sequence of edge pixels in $\mathbf{P}$ is defined by Eq. (10) to Eq. (12) [23]:

$$\mathbf{p}(u) = \sum_{i=0}^{n-1} \mathbf{p}_i g_i(u), \quad u \in [0, n-1], \tag{10}$$

$$g_i(u) = \frac{G_i(u)}{\sum_{j=0}^{n-1} G_j(u)}, \quad i = 0, ..., n-1, \tag{11}$$

$$G_i(u) = \sum_{j=-\infty}^{j=+\infty} \exp\left\{-\frac{[u-(u_i + jn)]^2}{2\sigma^2}\right\}, \tag{12}$$

where $g_i(u)$ are the basis functions of the curve, and $G_i(u)$ is a Gaussian of height and standard deviation σ centered at parameter u_i. The tangent direction θ at a curve point with parameter u is defined by Eq. (13) to Eq. (15) [23]:

$$\theta(u) = \arctan\left(\frac{dy(u)/du}{dx(u)/du}\right), \tag{13}$$

$$\frac{dx(u)}{du} = \frac{x(u+\delta u) - x(u-\delta u)}{2\delta u} \tag{14}$$

$$\frac{dy(u)}{du} = \frac{y(u+\delta u) - y(u-\delta u)}{2\delta u} \tag{15}$$

At this point, the orientation can be determined. In order to test the orientation identification ability of the polar microstructure, the relevant experiment was conducted. The image of the polar microstructure was rotated by six different angles: 0°, 45°, 60°, 80°, 90° and 180°. The abovementioned orientation algorithm was then used to calculate and display the orientation line of different images. Considering that the objective was mainly to contribute to length positioning measurement, the resolution of the algorithm was set as 0.1°. The experiment results are shown in Fig. 10, and it should be noticed that the orientation lines in Fig. 9 are all generated by calculation. The experimental results show that the calculated orientation agreed well with the actual values. The calculated results were for 0.0°, 45.0°, 60.0°, 80.0°, 90.0° and 180.0°. However, the resolution can be improved in the future by A+ [26], ANR [27], Zeyde [28], or other methods. In other words, the polar microstructure allows a feasible integrated method to be used to detect the angular displacement.

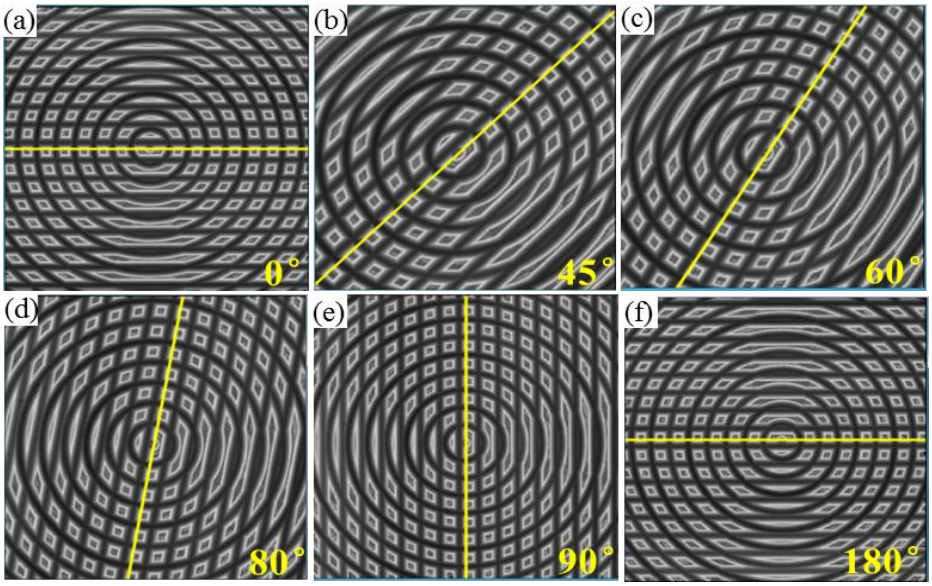

Fig. 10 Orientation detection of the polar microstructure

4.3 Resolution of pattern recognition

Template matching and sub-pixel interpolation methods were used to test the resolution of pattern recognition. Fig. 11 shows the experimental setup. The global image was the surface texture observed by the optical surface profiler (Zygo Nexview™ 3D Optical Surface Profiler); its actual area size was 1400 μm × 1400 μm with 924 pixels × 924 pixels. A template image was chosen from the midpoint area of the global image. The location was both the 331st pixel of the global image along X

and Y directions respectively. The actual area size of the template image was 400 μm × 400 μm with 264 pixels × 264 pixels. The matching process started from the top left corner of the global image and ended at its bottom right corner. The reference image had the same size as the template image, moving with each pixel step in the search region. During each moving step, the corresponding similarity between the reference image and template image was determined. Here, Normalized Cross Correlation (*NCC*) [29] was chosen as the indicator to describe the similarity which is expressed by Eq. (16) [17]:

$$NCC_{(u,v)} = \frac{\sum_{i=1}^{m}\sum_{j=1}^{n}[R(u+i,v+j)-\bar{R}(u,v)]\cdot[T(i,j)-\bar{T}]}{\left[\sum_{i=1}^{m}\sum_{j=1}^{n}(R(u+i,v+j)-\bar{R}(u,v))^2\right]^{\frac{1}{2}}\cdot\left[\sum_{i=1}^{m}\sum_{j=1}^{n}(T(i,j)-\bar{T})^2\right]^{\frac{1}{2}}} \tag{16}$$

where $R(u,v)$ represents the reference image of u^{th} row of v^{th} column and $R(u,v)$. $\bar{R}(u,v)$ is the grayscale average intensity of reference image $R(u,v)$, whereas $\bar{T}$ is the grayscale average intensity of template image T. These values are defined by Eq. (17) and Eq. (18) [17]:

$$\bar{R}(u,v) = \frac{1}{m\cdot n}\sum_{i=1}^{m}\sum_{j=1}^{n}R(u+i,v+j) \tag{17}$$

$$\bar{T} = \frac{1}{m\cdot n}\sum_{i=1}^{m}\sum_{j=1}^{n}T(i,j) \tag{18}$$

The NCC values are delivered between the interval [-1, 1], which means that if NCC = 1 the similarity is the best possible, whereas if NCC = -1 the template and the corresponding image are completely different. As a result, the point (u,v) which presents the best possible resemblance between R and T is defined by Eq. (19) and Eq. (20) [17]:

$$(u,v) = \arg\max_{(\hat{u},\hat{v})\in A} NCC(\hat{u},\hat{v}) \tag{19}$$

where,

$$A = \{(u,v)\,|\,1\le\hat{u}\le M-m, 1\le\hat{v}\le N-n\} \tag{20}$$

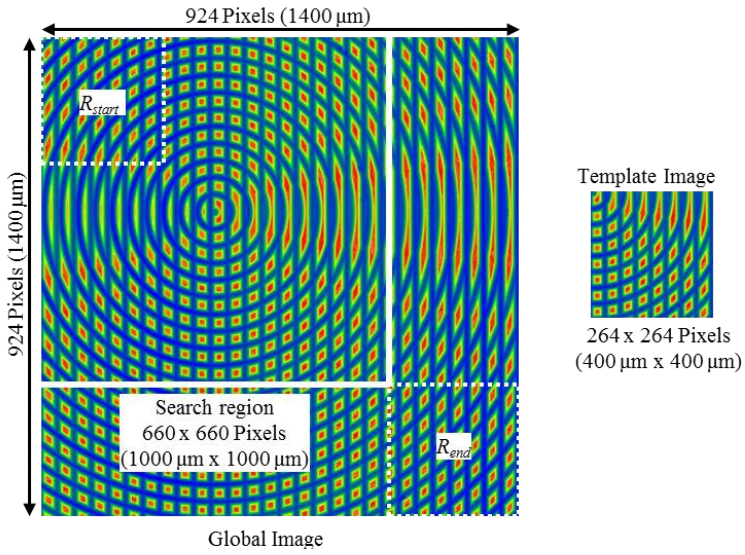

Fig.11 Experimental setup of the resolution and distinction rate test

All NCC value distribution after calculations in the searching region is shown in Fig. 12(a). The result shows that the NCC value creeps up at the midpoint ($u = 331, v = 331$, after Eq (3)) of the search region which indicates the largest similarity between the template image and reference image. In this experimental step, the calculated position was the same as the actual position of the template image. However, in general conditions, the movement distance is not an integer multiple of pixel size, but resolution is an important indicator to show the measurement accuracy. The current resolution of the matching method was calculated by $1400 / 924 = 1.515$ μm/pixel, which cannot achieve nanometer-level accuracy. Hence, sub-pixel interpolation needs to be conducted after determining u and v.

The pixel $(u = 331, v = 331)$ and its eight neighboring pixels totaling nine pixels were interpolated with the Bilinear Interpolation (BI) method [30]. After interpolation, each previous pixel was divided into smaller pixels with a higher resolution. In this experiment, the resolution changed from 1.51 μm/pixel to 9.35 nm/pixel. Further template matching was conducted among the sub-pixels. The NCC value distribution in the sub-pixel region is shown in Fig. 12(b). The experimental result shows that the NCC values still distributed differently in the sub-pixel region, and the closer to the center, the larger the value. The middlemost sub-pixel had the highest NCC value of 1.00. It should be noticed that the images in this experiment were generated by an interferometer whose original pixel size was 1.51 μm/pixel and achieved a resolution of 9.35 nm after sub-pixel interpolation. In future practical applications, polar microstructure will be observed with a

microscope whose original pixel size can achieve the 400 nm/pixel level. With the help of sub-pixel interpolation [26-28, 30], its final resolution could feasibly achieve 3 nm which means polar microstructures have a feature resolution of pattern recognition at the nanometer level.

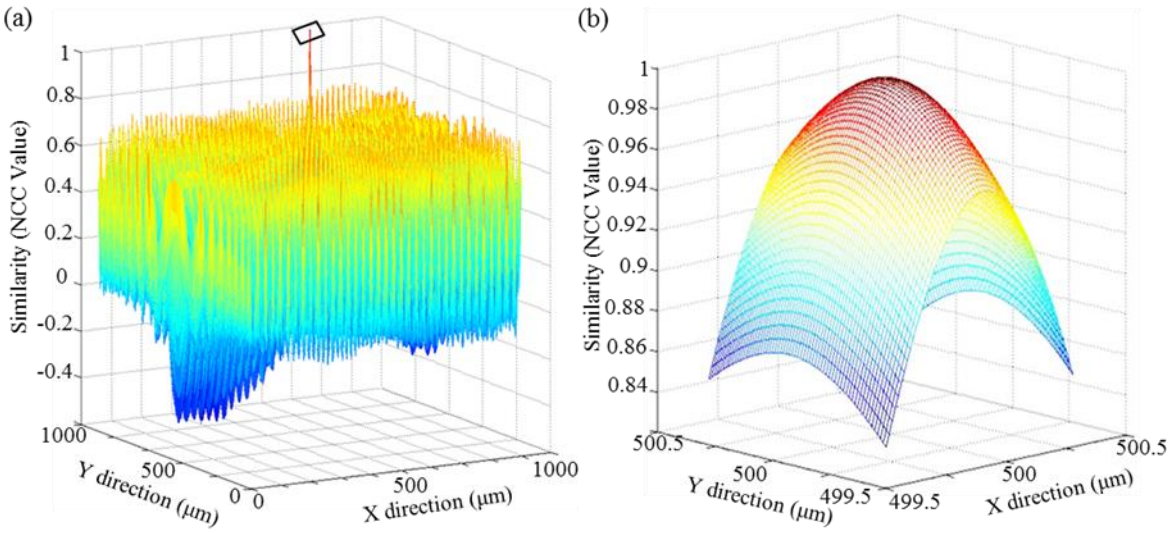

Fig. 12 NCC value distribution of different matching areas. (a) The global area (b) Enlarged area from Fig. 11(a) center which is near to the maximum similarity.

4.4 Global resolution of pattern recognition

In the previous experiments in section 4.3, the template image was a fixed choice which is not universal. To test the resolution of pattern recognition of the global polar microstructure surface, the template image was changed along the x and y directions in 10-μm steps. Fig. 13 shows the changing area with 400 μm × 400 μm, so a total of 1,681 template images were chosen. In each chosen template image, a repeated experiment as shown in Fig. 10 was conducted. The experimental steps were as follows:

1) Choose the template image;

2) Calculate all NCC values between the reference images with the chosen template image (see section 4.3);

3) Choose another template image and repeat Step 2 until 1,681 template images are obtained.

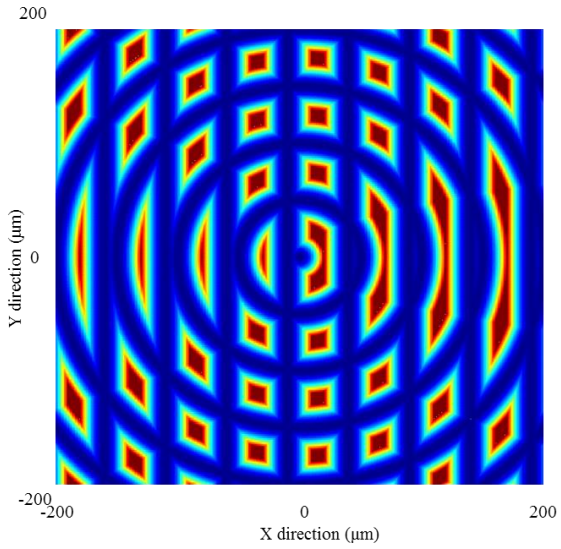

Fig. 13 Matchinig map

To judge the global pattern recognition performance of polar microstructures [31-33], this paper presents two criteria to judge it. One criterion is to consider the maximum degree of the mean, which is expressed by NCC_{max} / NCC_{mean}. The other criterion is to consider the maximum degree of highlighting in the secondary maximum, which is expressed by $\left(NCC_{max} - NCC_{2nd\ max}\right) / NCC_{2nd\ max}$. Using the abovementioned two criteria in each chosen template image aims to test the significance between the maximum value of NCC with both the average value of NCC and the second maximum value of NCC. NCC_{max} / NCC_{mean} is more inclined to indicate the design rationality of polar microstructures, while $\left(NCC_{max} - NCC_{2nd\ max}\right) / NCC_{2nd\ max}$ is more inclined to show the matching accuracy of polar microstructures using the NCC method. The larger NCC_{max} / NCC_{mean} and $\left(NCC_{max} - NCC_{2nd\ max}\right) / NCC_{2nd\ max}$ are, the more significant the resolution of pattern recognition is. The distribution of the values in the matching map is shown in Fig. 14. As shown in Fig. 14(a), the values of NCC_{max} / NCC_{mean} are all larger than 2 and the average value is 2.53. According to the recognized criteria [31], a value over 2 shows that the polar microstructure has good ability to be distinguished. According to Fig. 14(b), the values of $\left(NCC_{max} - NCC_{2nd\ max}\right) / NCC_{2nd\ max}$ are all larger than 0.05 and the average value is 0.18. This shows that NCC is a good indicator to express the resolution of pattern recognition. A large difference value of $\left(NCC_{max} - NCC_{2nd\ max}\right) / NCC_{2nd\ max}$ guarantees the accuracy of the NCC method.

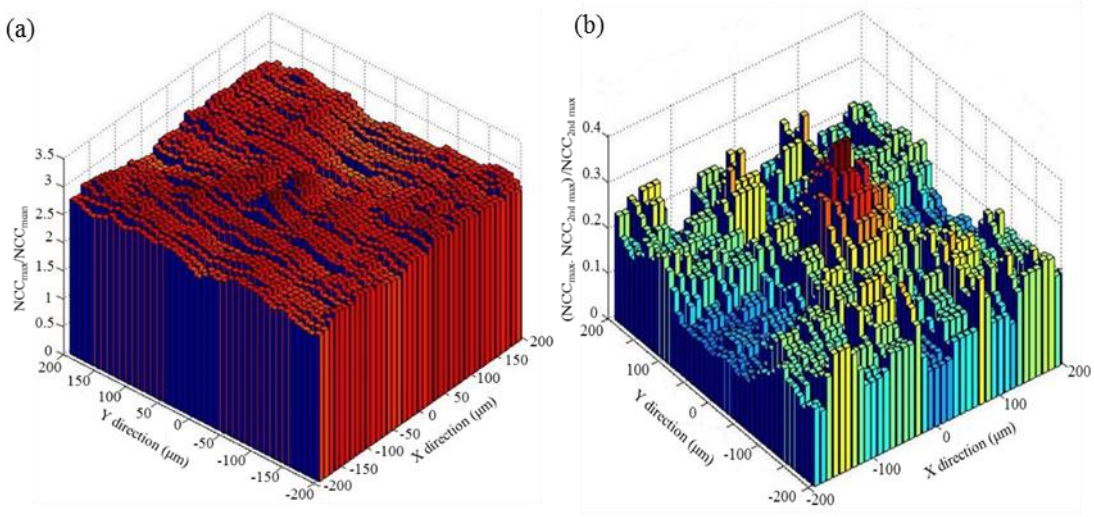

Fig. 14 The distribution of values in the matching map. (a) The values of (NCC_{max}/NCC_{mean}). (b) The values of ((NCC_{max}-$NCC_{2nd\ max}$)/$NCC_{2nd\ max}$)

Overall, the above validation experiments demonstrate the functional performance of polar microstructures. Its nanometer-level accuracy and feature resolution of pattern recognition show its feasibility to be applied in precision measurement, especially positioning on machine tools in the future.

5. Conclusion

In this paper, a polar microstructure achieving high resolution of pattern recognition is proposed. Generation of polar microstructures is based on the schematic diagram in the design of the process chain system in UPM. Also, the objectives and requirements in regard to computer vision are the consideration of feature point extraction, orientation, discrimination rate, etc. A polar microstructure was designed and fabricated based on the modeling of surface generation in UPM as well as the principles of image processing technology. To test the performance of the polar microstructure, a series of validation experiments was conducted such as feature point extraction, orientation test, resolution of pattern recognition, etc. The simulation experimental results show that the extraction of feature points is successful, and the orientation detection is feasible which will play an important role in angle displacement detection in the future. Moreover, the polar microstructure was able to achieve nanometer-level resolution of pattern recognition on the global map. The judging criteria for resolution of pattern recognition on global polar microstructure surface were also proposed and relevant simulations were conducted using the proposed criteria to validate the global resolution of pattern recognition performance of polar microstructures. In

conclusion, the performance of the polar microstructure demonstrates its feasibility for precision measurement and application for positioning of machine tools in the future.

Acknowledgement

The work described in this paper was mainly supported by a PhD studentship (project account code: RU7J) from The Hong Kong Polytechnic University.

References

[1] Gao, Wei, et al. Precision nano-fabrication and evaluation of a large area sinusoidal grid surface for a surface encoder. *Precision Engineering* 27.3 (2003): 289-298.

[2] Krolczyk, G. M., et al. Parametric and nonparametric description of the surface topography in the dry and MQCL cutting conditions. *Measurement* 121 (2018): 225-239.

[3] Krolczyk, Jolanta B., et al. Topographic inspection as a method of weld joint diagnostic. *Tehnicki vjesnik* 23.1 (2016): 301-306.

[4] Józwik, Jerzy, et al. Analysis of relation between the 3D printer laser beam power and the surface morphology properties in Ti-6Al-4V titanium alloy parts. Journal of the Brazilian *Society of Mechanical Sciences and Engineering*40.4 (2018): 215.

[5] Forsyth, David A., and Jean Ponce. *Computer vision: a modern approach*. Prentice Hall Professional Technical Reference, 2002.

[6] Rautaray, Siddharth S., and Anupam Agrawal. "Vision based hand gesture recognition for human computer interaction: a survey." *Artificial Intelligence Review* 43.1 (2015): 1-54.

[7] Szegedy, Christian, et al. "Rethinking the inception architecture for computer vision." *Proceedings of the IEEE Conference on Computer Vision and Pattern Recognition*. 2016.

[8] Tanimoto, Steven, ed. *Structured computer vision: machine perception through hierarchical computation structures*. Elsevier, 2014.

[9] Schroff, Florian, Dmitry Kalenichenko, and James Philbin. "Facenet: A unified embedding for face recognition and clustering." *Proceedings of the IEEE conference on computer vision and pattern recognition*. 2015.

[10] Quine, Brendan M., et al. "Determining star-image location: A new sub-pixel interpolation technique to process image centroids." *Computer Physics Communications* 177.9 (2007): 700-706.

[11] Lipton, Alan J., Hironobu Fujiyoshi, and Raju S. Patil. "Moving target classification and tracking from real-time video." *Applications of Computer Vision, 1998. WACV'98. Proceedings., Fourth IEEE Workshop on*. IEEE, 1998.

[12] Boneh, Dan, Amit Sahai, and Brent Waters. "Functional encryption: a new vision for public-key cryptography." *Communications of the ACM* 55.11 (2012): 56-64.

[13] Bay, Herbert, et al. "Speeded-up robust features (SURF)." *Computer vision and image understanding* 110.3 (2008): 346-359.

[14] Rosten, Edward, and Tom Drummond. "Machine learning for high-speed corner detection." *European conference on computer vision*. Springer, Berlin, Heidelberg, 2006.

[15] Wang, Xiaoxian, et al. "A computer-vision-based rotating speed estimation method for motor bearing fault diagnosis." *Measurement Science and Technology* 28.6 (2017): 065012.

[16] Zhao, Chenyang, Chi Fai Cheung, and Mingyu Liu. "Modeling and Simulation of a Machining Process Chain for the Precision Manufacture of Polar Microstructure." *Micromachines* 8.12 (2017): 345.

[17] Zhao, Chenyang, Chifai Cheung, and Mingyu Liu. "Integrated polar microstructure and template-matching method for optical position measurement." *Optics Express* 26.4 (2018): 4330-4345.

[18] Zhao, C., C. F. Cheung, and L. Kong. "A study of optimization of machining strategy for enhancing the efficiency of process chain in ultra-precision machining." (2016).

[19] Zhao, Chenyang, and Chi Fai Cheung. "Theoretical and experimental investigation of the effect of the machining process chain on surface generation in ultra-precision fly cutting." The International Journal of Advanced Manufacturing Technology (2018): 1-13.

[20] Chen, Shanshan, et al. "Simulated and measured surface roughness in high-speed grinding of silicon carbide wafers." *The*

International Journal of Advanced Manufacturing Technology 91.1-4 (2017): 719-730.

[21] Schweitzer, H., Bell, J. W., & Wu, F. (2002, May). Very fast template matching. In European Conference on Computer Vision (pp. 358-372). Springer, Berlin, Heidelberg.

[22] Grisan, E., Poletti, E., & Ruggeri, A. (2009). An improved segmentation of chromosomes in Q-band prometaphase images using a region based level set. In World Congress on Medical Physics and Biomedical Engineering, September 7-12, 2009, Munich, Germany (pp. 748-751). Springer, Berlin, Heidelberg.

[23] Goshtasby, Arthur Ardeshir. Theory and Applications of Image Registration. John Wiley & Sons, 2017.

[24] Canny, John. "A computational approach to edge detection." *Readings in Computer Vision*. 1987. 184-203.

[25] Dollár, Piotr, and C. Lawrence Zitnick. "Fast edge detection using structured forests." *IEEE transactions on pattern analysis and machine intelligence* 37.8 (2015): 1558-1570.

[26] Timofte, R., De Smet, V., & Van Gool, L. (2014, November). A+: Adjusted anchored neighborhood regression for fast super-resolution. In Asian Conference on Computer Vision (pp. 111-126). Springer, Cham.

[27] Timofte, R., De, V., & Van Gool, L. (2013, December). Anchored neighborhood regression for fast example-based super-resolution. In Computer Vision (ICCV), 2013 IEEE International Conference on (pp. 1920-1927). IEEE.

[28] Zeyde, R., Elad, M., & Protter, M. (2010, June). On single image scale-up using sparse-representations. In International conference on curves and surfaces (pp. 711-730). Springer, Berlin, Heidelberg.

[29] Lewis, J. P. (1995, May). Fast normalized cross-correlation. In Vision interface (Vol. 10, No. 1, pp. 120-123).

[30] Gribbon, K. T., & Bailey, D. G. (2004, January). A novel approach to real-time bilinear interpolation. In Electronic Design, Test and Applications, Proceedings. DELTA 2004. Second IEEE International Workshop on (pp. 126-131). IEEE.

[31] Clausi, D. A., & Deng, H. (2005). Design-based texture feature fusion using Gabor filters and co-occurrence probabilities. IEEE Transactions on Image Processing, 14(7), 925-936.

[32] Weldon, T. P., Higgins, W. E., & Dunn, D. F. (1996). Efficient Gabor filter design for texture segmentation. Pattern Recognition, 29(12), 2005-2015.

[33] Li, M., & Staunton, R. C. (2008). Optimum Gabor filter design and local binary patterns for texture segmentation. Pattern Recognition Letters, 29(5), 664-672